Progress In Electromagnetics Research, Vol. 129, 109–123, 2012

QUANTITATIVE COMPARISON OF FLUX-MODULATED INTERIOR PERMANENT MAGNET MACHINES WITH DISTRIBUTED WINDINGS AND CONCENTRATED WINDINGS

G. Xu[1, 3], L. Jian[1, 2, *], W. Gong[1, 4], and W. Zhao[4]

[1]The Chinese University of Hong Kong, Sha Tin, Hong Kong, China

[2]Shenzhen Institutes of Advanced Technology, Chinese Academy of Sciences, 1068 Xueyuan Avenue, University Town, Shenzhen, China

[3]Department of Electrical Engineering, Tongji University, Shanghai, China

[4]School of Electrical and Information Engineering, Jiangsu University, No. 301, Xuefu Road, Zhenjiang, China

Abstract—Low speed flux-modulated permanent magnet machines (FMPMs) which are based on 'magnetic-gearing effect' have attracted increasing attention due to their high torque capability and simple structure. In order to assess the potentials of FMPMs in the application of low-speed direct-drive, two flux-modulated interior PM machines with distributed windings and concentrated windings are quantitatively compared by using finite element method. The results demonstrate that the machine with distributed windings can offer higher peak electromagnetic torques and lower torque ripples. Moreover, the machine with distributed windings also present stronger flux-weakening capability and lower power losses. The results also indicates that the magnetic saturation problem should be paid full attention when design flux-modulated interior PM machine with concentrated windings. If this problem can be well solved, the performance of machine with concentrated windings may be improved.

Received 9 April 2012, Accepted 4 June 2012, Scheduled 13 June 2012

* Corresponding author: Linni Jian (ln.jian@siat.ac.cn).

1. INTRODUCTION

Most recently, the low-speed PM machines based on the magnetic-gearing effect (or 'flux-modulation effect') has become very attractive. In magnetic gears (MGs) [1–4], abundant asynchronous flux harmonics can be produced by the field modulation arising from the non-even magnetic field path. With the interaction of the specific harmonics [5], both torque transmission and speed variation can be achieved. In [6], an integrated magnetic-geared machine (IMGM) was proposed, in which a PM high-speed brushless machine was integrated into the inner bore of a MG to realize low-speed operation. In [7], a 'pseudo' direct-drive machine was proposed, in which the armature windings are deployed along with the multi-pole PMs on the periphery of the modulating ring of the MG, and the modulating ring is connected to output shaft to offer low-speed rotation. In [8], a new IMGM was proposed, in which the armature windings are directly deployed into the air slots adjacent to the modulating segments. Although these machines present very high torque density, they are hurdled by the complicated physical structures due to the double rotary parts. Inspired by the IMGM, a flux-modulated PM machine (FMPM) was proposed in [9], in which the high speed rotor existing in the IMGM was removed, and the asynchronous flux harmonics are directly coupled with the armature windings. In the FMPM presented in [10], the flux-modulation poles are equipped on the stator. Thus, only one air gap is needed. Moreover, the concentrated armature windings are employed. Actually, the FMPMs can be tracked back to a decade ago. The so-called vernire machines are also based on the flux-modulation effect [11]. What they differ from the machine presented in [10] lies in that they usually employ distributed windings.

In order to assess the potentials of the FMPMs in the application of low-speed direct-drive, this paper is devoted to compare two flux-modulated interior PM Machines, one is with concentrated windings and the other is with distributed windings. Considering the demands of practical applications, such as electric vehicles, the comparison will focus on the aspects of torque characteristics, flux-weakening capability and power losses. The finite element analysis (FEA) will be engaged to conduct quantitative comparisons. It has been extensively used as an effective tool to estimate the overall performance of electric machines [12–17]. The results and conclusions drawn in this paper will help enrich the knowledge on FMPMs.

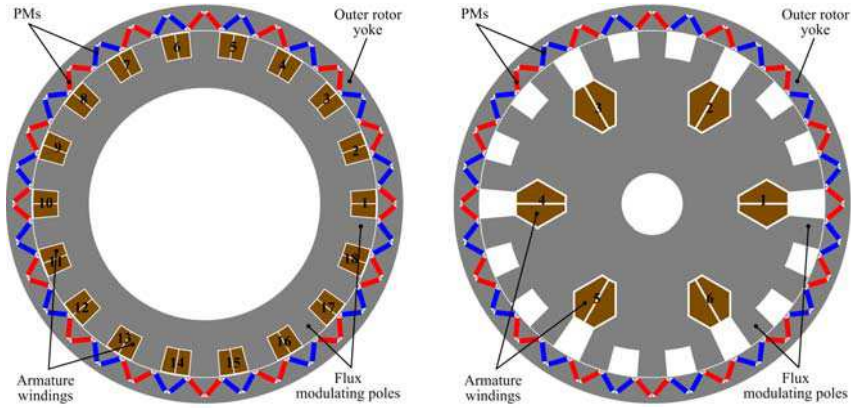

Figure 1. Flux-modulated interior PM machines. (a) Machine I: with distributed windings. (b) Machine II: with concentrated windings.

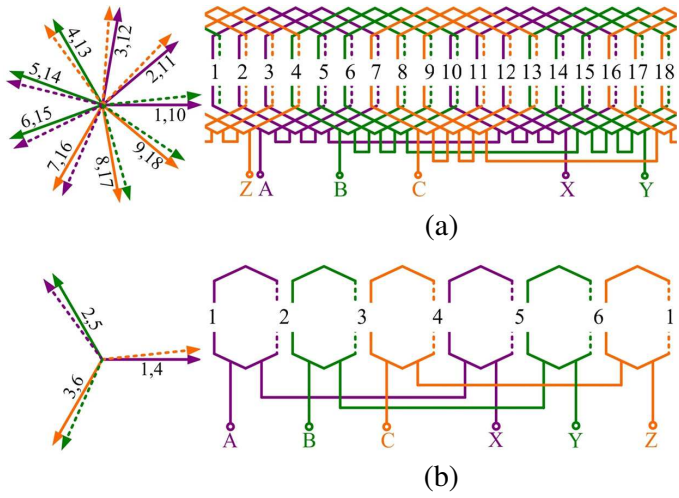

Figure 2. Winding connections. (a) Machine I. (b) Machine II.

2. FLUX-MODULATED INTERIOR PERMANENT MAGNET MACHINES AND THEIR OPERATING PRINCIPLE

Figure 1 shows the cross section views of the two flux-modulated interior PM machines. Both machines are with outer-rotor topology.

Table 1. Structural sizes of flux-modulated interior PM machines.

Outside radius of outer-rotor	195 [mm]
Inside radius of outer-rotor	170 [mm]
Length of airgap	0.8 [mm]
Outside radius of inner-stator	169.2 [mm]
Length of PMs	19.1 [mm]
Thickness of PMs	5 [mm]
Axial length	110 [mm]
Area of each armature slot in Machine I	701.3 [mm^2]
Area of each armature slot in Machine II	1767.4 [mm^2]

Moreover, the two rotors have exactly the same constitution, in which interior PMs are employed, and their pole-pair number (PPN) P_r equals 16. The flux modulating poles (FMPs) are equipped on the stator, and the numbers of FMPs N_f are both equal to 18 for the two machines. For fair comparison, the size and shape of the airgap and FMPs are also the same in the two machines. The main difference between these two machines lies in the armature windings. In machine I, the three-phase distributed windings are deployed in the 18 air-slots adjacent to the FMPs. While, in machine II, the three-phase concentrated windings are equipped in the 6 air-slots that are fabricated inside the FMPs. Figure 2 illustrates the winding connections of the two machines. They both adopt double-layer armature windings, and their PPN P_s equals 2. The structural sizes are listed in Table 1.

In traditional PM machines, the PPN of armature windings is designed to be equal to the PPN of PMs, so that the electro-mechanical energy conversion can be achieved by the interaction of fundamental components of the magnetic fields excited by the PMs and the armature currents. Nevertheless, the PPN of the armature windings is not equal to that of the PM poles in FMPMs. Their operating principle relies on the flux modulating effect arising from the non-even magnetic field path caused by the FMPs. After modulation, the magnetic field in the airgap is compounded by a series of harmonic components. The PPNs of the harmonic component $H_r\,(i,j)$ excited by the rotor PMs can be determined by [5]:

$$P(i,j) = |iP_r + jN_f| \tag{1}$$

where $i = 1, 2, 3, \ldots, \infty$ and $j = 0, \pm 1, \pm 2, \pm 3, \ldots, \pm\infty$, and the

corresponding rotational speed can be given by:

$$\omega(i,j) = \frac{iP_r}{iP_r + jN_f}\omega_r \tag{2}$$

where ω_r is the rotational speed of the outer-rotor.

Similarly, the PPNs of the harmonic component $H_s(i,j)$ excited by the armature windings can be determined by [5]:

$$P'(i,j) = |iP_s + jN_f| \tag{3}$$

and the corresponding rotational speed is given by:

$$\omega'(i,j) = \frac{iP_s}{iP_s + jN_f}\omega_s \tag{4}$$

where ω_s is the rotational speed of the electromagnetic flux vector.

When designing FMPMs, the following relationships should be satisfied [5]:

$$N_f = P_r + P_s \tag{5}$$

$$\omega_s = -\frac{P_r}{P_s}\omega_r \tag{6}$$

Here in (6), the minus notation means that the electromagnetic flux vector should rotate in the opposite position with that of the rotor. From (1)–(6), it can be known that the harmonic component $H_r(1,-1)$ excited by the rotor PMs and the harmonic component $H_s(1,0)$ excited by the armature windings are with the same PPN (PPN = 2) and the same rotational speed. Thus, stable electromechanical energy conversion can be achieved by the interaction of harmonics $H_r(1,-1)$ and $H_s(1,0)$. What is more, the harmonic component $H_r(1,0)$ excited by the rotor PMs and the harmonic component $H_s(1,-1)$ excited by the armature windings also have contribution to the stable electromechanical energy conversion, since they are with the same PPN (PPN = 16) and the same rotational speed as well.

Figure 3 shows the flux distributions at no-load. The harmonics with PPN = 2 can be clearly observed on the stator yokes. Figure 4 shows the no-load back electromotive force (EMF) waveforms when rotating at 1000 rpm, the number of conductors in each coil is chosen to be 1 for both machines. It can be found that the back EMF of machine I is much more sinusoidal than that of machine II. This is a well-known merit of distributed windings over concentrated windings.

3. TORQUE CHARACTERISTICS

3.1. Torque Capacity

The peak electromagnetic torques are determined by keeping the rotors still, and injecting balanced three-phase currents to the armature

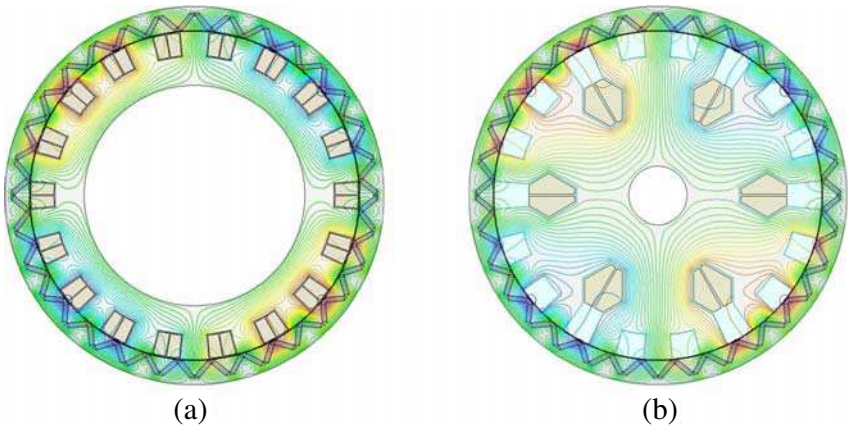

Figure 3. Flux distribution at no-load. (a) Machine I. (b) Machine II.

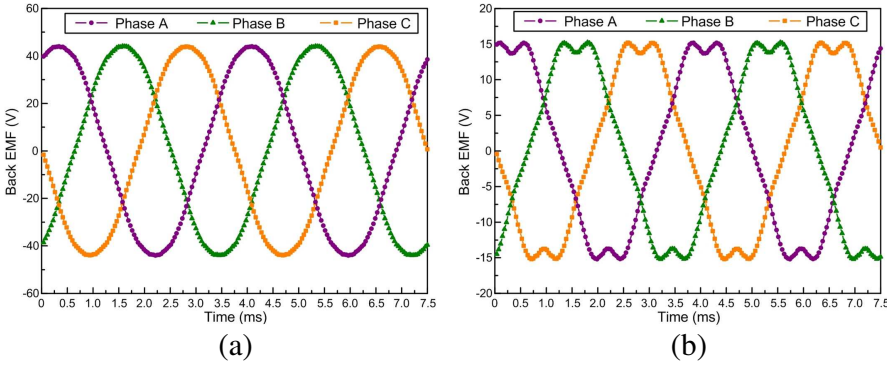

Figure 4. Back EMF waveforms at no-load with $\omega_r = 1000\,\text{rpm}$. (a) Machine I. (b) Machine II.

windings. Figures 5(a) and (b) illustrates the torque-time curves in a complete cycle with different current densities. The slot fill factors are chosen as 0.7 for both machines. It can be observed that the waveforms obtained from machine I is much more sinusoidal than that obtained form machine II. This implies that the machine I can offer much less torque ripples than machine II. Next in Figure 5(c), the peak electromagnetic torques with different current densities are compared. It can be found that machine I can offer higher peak torques than machine II. When the current density $J = 2.5\,\text{A/mm}^2$, the peak torques offered by machine I and II are 324.75 Nm and 267.23 Nm,

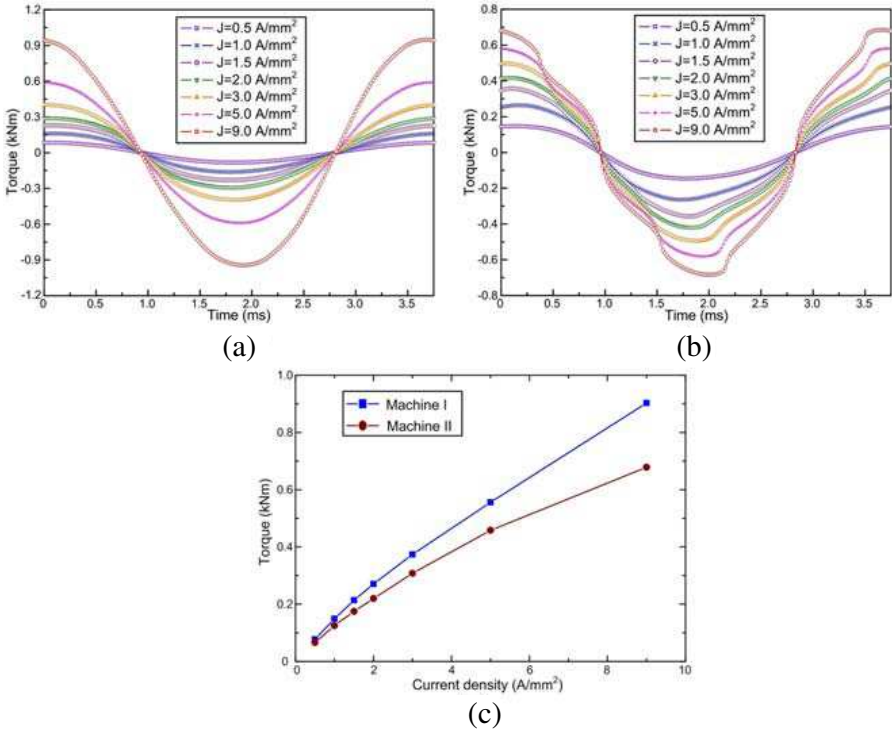

Figure 5. Torque capacity. (a) Torque-time curves of machine I. (b) Torque-time curves of machine II. (c) Peak electromagnetic torques with different current densities.

respectively. While, when the current density $J = 5.0\,\mathrm{A/mm^2}$, the peak torques offered by machine I and II are 556.60 Nm and 454.32 Nm, respectively. Herein, the rated current density is chosen as $2.5\,\mathrm{A/mm^2}$ out of the consideration for both temperature rising and magnetic saturation, which will be elaborated later.

3.2. Impact of Magnetic Saturation

It had been thought that in machine II with concentrated windings, the slots for containing armature conductors could be designed freely to achieve prominent performance over machine I, such as higher peak electromagnetic torque than machine I. However, we found that the adoption of concentrated windings will inevitably cause serious magnetic saturation problem. In our initial design of machine II, the area of the armature slot is much bigger, so that the conductors can

carry higher armature current than machine I. However, due to the deep magnetic saturation, machine II did not offer higher than machine I as expected. Moreover, the magnetic saturation will result in high power losses and waste of winding materials. Thus, we optimized the design of machine II and the armature slots are reduced. In addition, magnetic saturation of iron yokes will cause the distortions of back EMF waveforms. Figure 6 shows the back EMF waveforms of Phase-A when current density, rotational speed and number of conductor per coil are 5.0 A/mm^2, 1000 rpm and 1, respectively. The laminated

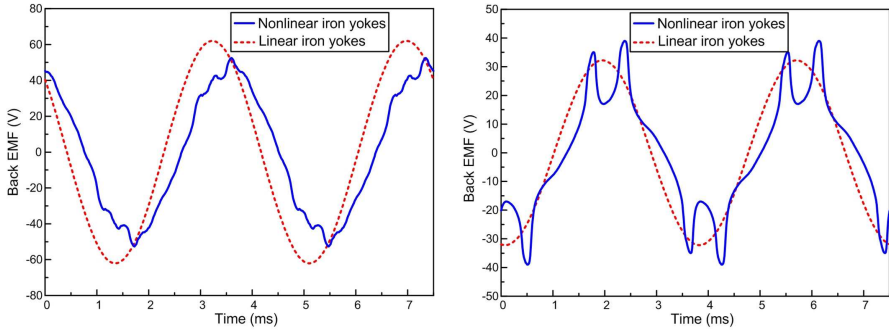

Figure 6. Back EMF waveforms with $J = 5.0\,\mathrm{A/mm^2}$ and $\omega_r = 1000\,\mathrm{rpm}$. (a) Machine I. (b) Machine II.

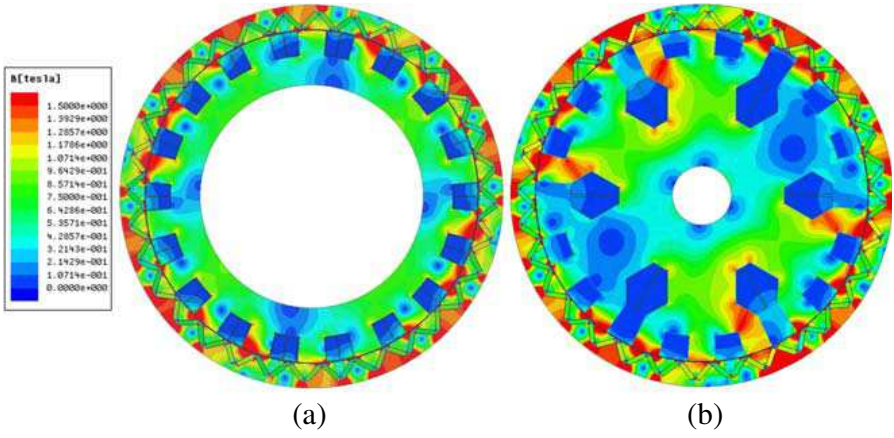

Figure 7. Flux density distribution with $J = 5.0\,\mathrm{A/mm^2}$. (a) Machine I. (b) Machine II.

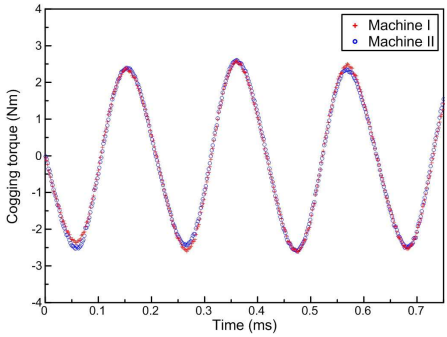

Figure 8. Cogging torque waveforms.

silicon steel (Type 50H470) is engaged for the iron yokes. It can be observed that the waveform of machine II is seriously distorted. With the increase of armature current, the iron yoke becomes deeply saturated, and the magnetic permeability decrease rapidly. This will arouse the spikes in back EMF waveforms. To bear this out, the iron yokes are assumed to be linear materials, and it can be observed that the spikes are disappeared. The distortion of back EMF waveform could cause several problems, such as low power factor and uncertain demand for the DC link voltage, which bring in much trouble for designing power electronic drivers. Figure 7 illustrates the flux density distributions in the two machines when the current in Phase-A reaches its peak value. It can be observed that the saturation problem in machine with concentrated windings is much more serious than that in machine with distributed windings.

3.3. Cogging Torque and Torque Ripples

Figure 8 shows the cogging torque waveforms of the two machines. Since the alignment of PMs and the shape of the FMPs are exactly the same in the two machines, their cogging torques are no different from each other. The peak values are less than 3 Nm. Considering that the rated electromagnetic torques for both machines are around 300 Nm, the cogging torques exhibited here are satisfactorily low in these two cases.

In order to figure out the torque ripples of the two machine, the rotors are set to synchronously rotate with the electromagnetic flux linkage vectors. Figure 9 illustrates the resulted torque-time waveforms with different current densities, and the ratios between the magnitudes of the torque ripples and the corresponding average torques are also

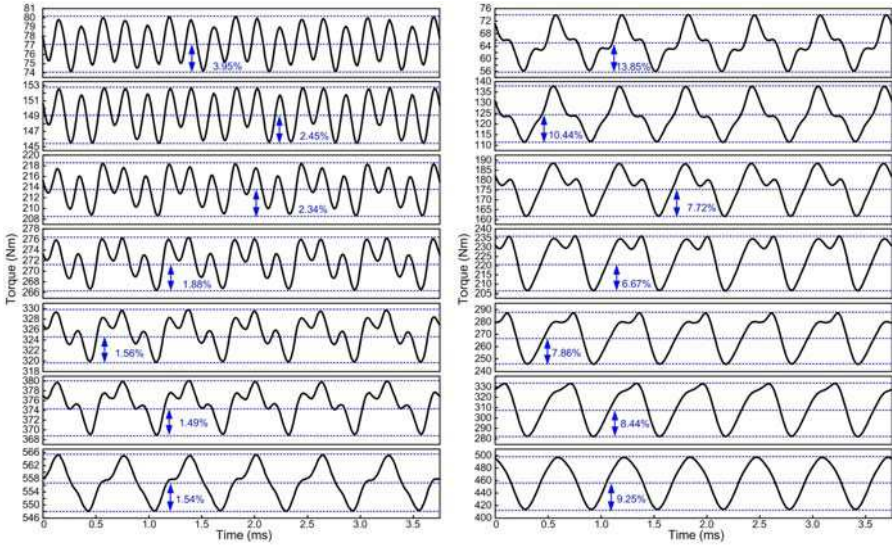

Figure 9. Torque ripples. From top to bottom: current density equals 0.5, 1.0, 1.5, 2.0, 2.5, 3.0 and 5.0 A/mm^2. (a) Machine I. (b) Machine II.

indicated. Apparently, the torque ripples in machine II is much more serious than that in machine I.

4. FLUX-WEAKENING CAPABILITY

For fair comparison, the rated speed and the rated phase voltage (peak value) are chosen as 1000 rpm and 400 V for both machines. Therefore, the resulted numbers of conductor per coil are 9 and 17 for machine I and machine II, and the phase resistances are 0.0015 Ω and 0.0050 Ω for machine I and II, respectively. Once the machines run beyond their rated speeds, the armature fields should be employed to weaken the flux in airgap, so as to fulfill the limit of the phase voltage. In Figure 10, the peak values of the phase voltage and the produced electromagnetic torques with different current phase angles (Phase-A) are shown. It can be observed that when the current phase angle is less than 90 degree, the peak value of phase voltage goes down with the increase of the current phase angle, and the produced electromagnetic torques are positive; while, when the peak current phase angle is bigger than 90 degree, the peak value of phase voltage goes up with the increase

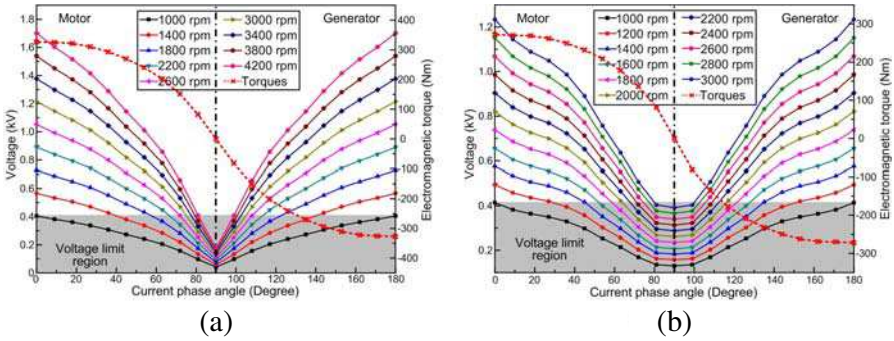

Figure 10. Voltage and electromagnetic torque versus current phase angle. (a) Machine I. (b) Machine II.

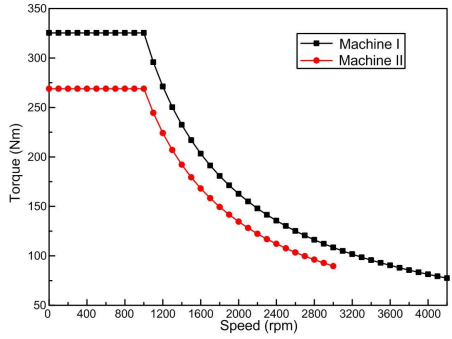

Figure 11. Torque-speed envelopes.

of the current phase angle, and the machines are outputting negative electromagnetic torques which means they are working with generation mode, such as regenerative braking. Moreover, the zones in shadow are the voltage limit regions. With the increase of the rotation speed, the feasible interval of the current phase angle becomes very narrow, and the produced electromagnetic torque turns to be very low. Finally, the torque-speed envelops of the two machines can be determined as shown in Figure 11. Through flux-weakening, the maximum speeds of the constant-power operation can reach 4200 rpm and 3000 rpm for machine I and II, respectively. And, machine I presents stronger flux-weakening capability than machine II.

5. POWER LOSSES

Power losses mainly include the copper loss in windings and the iron losses in iron yokes [18]. Power losses could be very different at the different working points, and they are also impacted by the drive control method. Herein, we have chosen several typical working points which are located on the envelops illustrated in Figure 11 for assessing the power losses in the two machines. All the selected working points are located on the torque-speed envelopes shown in Figure 11: In the constant-torque region, four points with rotational speeds equal to 250 rpm, 500 rpm, 750 rpm and 1000 rpm are selected for both machines; While in the constant-power region, two points with rotational speeds equal to 2000 rpm and 3000 rpm are selected for machine II, three points with rotational speeds equal to 2000 rpm, 3000 rpm and 4200 rpm are selected for machine I. Figure 12 illustrates the iron losses versus time curves at the selected working points. It can be found that after about 1 ms, the eddy currents have been fully

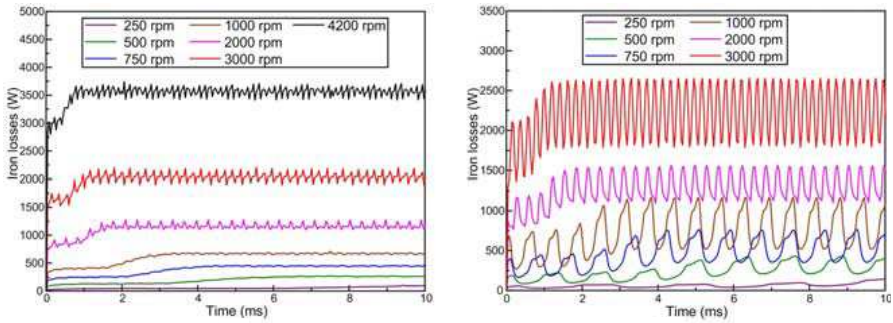

Figure 12. Iron losses. (a) Machine I. (b) Machine II.

Table 2. Power losses and efficiency.

Speed [rpm]	250	500	750	1000	2000	3000	4200
Copper loss (I) [W]	39.5	39.5	39.5	39.5	39.5	39.5	39.5
Copper loss (II) [W]	19.1	19.1	19.1	19.1	19.1	19.1	Nil
Iron loss (I) [W]	112.4	262.9	448.7	671.2	1162.5	2038.9	3566.1
Iron loss (II) [W]	129.4	308.9	531.3	802.3	1311.9	2244.3	Nil
Efficiency (I) [%]	98.25	98.26	98.13	97.96	96.60	94.25	90.43
Efficiency (II) [%]	97.93	97.72	97.46	97.17	95.49	92.56	Nil

established, and the iron losses curves enter into the stable stage. It can also be observed that the fluctuation in iron losses curves of machine II is much more fierce than that of machine I. This is mainly caused by the abundant asynchronous harmonics in the armature field produced by the concentrated windings.

The calculated copper loss, iron losses and efficiency are listed in Table 2. The copper loss in machine I is stronger than that in machine II, but the iron losses in machine I is weaker than that in machine II. Since the iron losses are dominant over copper loss, the efficiency of machine I is a little bit higher than that of machine II.

6. CONCLUSIONS

In this paper, the performances of flux-modulated interior PM machines with distributed windings and concentrated windings are comprehensively compared, and the following conclusions can be reached:

1) With the same current density, the machine with distributed windings can offer higher peak electromagnetic torque than the machine with concentrated windings.

2) The torque ripples in machine with concentrated windings are much more serious than that in machine with distributed windings due to the abundant asynchronous harmonics in the armature field produced by the concentrated windings.

3) The flux-weakening capability of machine with distributed windings is stronger than that of machine with concentrated windings.

4) The power losses in machine with distributed windings are lower than that in machine with concentrated windings. Therefore, the efficiency of machine with distributed windings is higher than that of machine with concentrated windings.

It is worth noting that the magnetic saturation problem should be paid full attention when designing the flux-modulated interior PM machine with concentrated windings. If this problem can be well solved by using methods such as optimizing the number of armature slots and the pole-pair numbers of the windings, the performances of this machine may be improved, since its armature slots can be designed freely, not like those in the machine with distributed windings.

ACKNOWLEDGMENT

This work was supported by a grant (Project No. 51107141) from the National Natural Science Foundation of China.

REFERENCES

1. Rasmussen, P., T. Andersen, F. Jorgensen, and O. Nielsen, "Development of a high-performance magnetic gear," *IEEE Trans. Ind. Appl.*, Vol. 41, No. 3, 764–770, 2005.
2. Jian, L., K. T. Chau, Y. Gong, J. Jiang, C. Yu, and W. Li, "Comparison of coaxial magnetic gears with different topologies," *IEEE Trans. Magn.*, Vol. 45, No. 10, 4526–4529, 2009.
3. Jian, L. and K.-T. Chau, "Analytical calculation of magnetic field distribution in coaxial magnetic gears," *Progress In Electromagnetics Research*, Vol. 92, 1–16, 2009.
4. Lubin, T., S. Mezani, and A. Rezzoug, "Analytical computation of the magnetic field distribution in a magnetic gear," *IEEE Trans. Magn.*, Vol. 46, No. 7, 2611–2621, 2010.
5. Jian, L. and K. T. Chau, "A coaxial magnetic gear with Halbach permanent-magnet arrays," *IEEE Trans. Energy Conversion*, Vol. 25, No. 2, 319–328, 2010.
6. Jian, L., K. T. Chau, and J. Jiang, "A magnetic-geared outer-rotor permanent-magnet brushless machine for wind power generation," *IEEE Trans. Ind. Appl.*, Vol. 45, No. 3, 954–962, 2009.
7. Atallah, K., J. Rens, S. Mezani, and D. Howe, "A novel pseudo direct-drive brushless permanent magnet machine," *IEEE Trans. Magn.*, Vol. 44, No. 11, 4349–4352, 2008.
8. Jian, L., G. Xu, Y. Gong, J. Song, J. Liang, and M. Chang, "Electromagnetic design and analysis of a novel magnetic-gear-integrated wind power generator using time-stepping finite element method," *Progress In Electromagnetics Research*, Vol. 113, 351–367, 2011.
9. Wang, L., J. Shen, P. Luk, W. Fei, C. Wang, and H. Hao, "Development of a magnetic-geared permanent-magnet brushless motor," *IEEE Trans. Magn.*, Vol. 45, No. 10, 4578–4581, 2009.
10. Li, J., K. T. Chau, J. Jiang, C. Liu, and W. Li, "A new efficient permanent-magnet vernier machine for wind power generation," *IEEE Trans. Magn.*, Vol. 46, No. 6, 1475–1478, 2010.
11. Toba, A. and T. Lipo, "Generic torque-maximizing design methodology of surface permanent-magnet vernier machine," *IEEE Trans. Ind. Appl.*, Vol. 36, No. 6, 1539–1546, 2000.
12. Jian, L. and K.-T. Chau, "Design and analysis of a magnetic-geared electronic-continuously variable transmission system using finite element method," *Progress In Electromagnetics Research*, Vol. 107, 47–61, 2010.

13. Touati, S., R. Ibtiouen, O. Touhami, and A. Djerdir, "Experimental investigation and optimization of permanent magnet motor based on coupling boundary element method with permeances network," *Progress In Electromagnetics Research*, Vol. 111, 71–90, 2011.
14. Lecointe, J.-P., B. Cassoret, and J. Brudny, "Distinction of toothing and saturation effects on magnetic noise of induction motors," *Progress In Electromagnetics Research*, Vol. 112, 125–137, 2011.
15. Mahmoudi, A., N. Rahim, and H. Ping, "Axial-flux permanent-magnet motor design for electric vehicle direct drive using sizing equation and finite element analysis," *Progress In Electromagnetics Research*, Vol. 122, 467–496, 2012.
16. Zhao, W., M. Cheng, R. Cao, and J. Ji, "Experimental comparison of remedial single-channel operations for redundant flux-switching permanent-magnet motor drive," *Progress In Electromagnetics Research*, Vol. 123, 189–204, 2012.
17. Mahmoudi, A., S. Kahourzade, N. Rahim, and H. Ping, "Improvement to performance of solid-rotor-ringed line-start axial-flux permanent-magnet motor," *Progress In Electromagnetics Research*, Vol. 124, 383–404, 2012.
18. Roshen, M., "Iron loss model for permanent-magnet synchronous motors," *IEEE Trans. Magn.*, Vol. 43, No. 8, 3428–3434, 2007.